

Article

Fluorine Free Surface Modification of Microfibrillated Cellulose-Clay Composite Films: Effect of Hydrophobicity on Gas Barrier Performance

Mohammed Arif Poothanari ^{1,2,*} and Yves Leterrier ¹ 

¹ Laboratory for Processing of Advanced Composites (LPAC), Ecole Polytechnique Fédérale de Lausanne (EPFL), CH-1015 Lausanne, Switzerland; yves.leterrier@epfl.ch

² Department of Physics, MES College Nedumkandam, Idukki Township 685553, Kerala, India

* Correspondence: arif@mesnedumkandam.in

Abstract: Diffusion barrier composite films based on microfibrillated cellulose (MFC) and clay were developed with attention paid to the influence of thermal annealing and a fluorine-free surface silylation on their microstructure, water contact angle (WCA), mechanical properties, oxygen transmission rate (OTR), and water vapor transmission rate (WVTR). The OTR of MFC at 23 °C increased from 1.2 to 25.3 cm³/m²/day/bar as relative humidity increased from 50% to 80%. Annealing increased the film's crystallinity, surface roughness, and hydrophobicity, while decreasing its OTR by 20% at 80%RH. The addition of clay led to a 30% decrease of OTR at 80%RH due to partial exfoliation and to a 50% decrease when combined with annealing. Silylation increased the hydrophobicity of surface of the film and its combination with clay and annealing led to a WCA of 146.5°. The combination of clay, annealing, and silylation considerably reduced the OTR at 80%RH to a value of 8 cm³/m²/day/bar, and the WVTR at 23 °C and 50%RH from 49 g/m²/day for MFC to 22 g/m²/day. The reduction of OTR and WVTR was found to correlate with the increase in surface hydrophobicity of the film, which was attributed to the reduced access of water molecules within the MFC network.

Keywords: microfibrillated cellulose; clay; heat-treatment; silane; oxygen permeation; water vapor permeation; hydrophobic



Citation: Poothanari, M.A.; Leterrier, Y. Fluorine Free Surface Modification of Microfibrillated Cellulose-Clay Composite Films: Effect of Hydrophobicity on Gas Barrier Performance. *Surfaces* **2024**, *7*, 283–295. <https://doi.org/10.3390/surfaces7020019>

Academic Editor: Gaetano Granozzi

Received: 19 February 2024

Revised: 13 April 2024

Accepted: 27 April 2024

Published: 1 May 2024



Copyright: © 2024 by the authors. Licensee MDPI, Basel, Switzerland. This article is an open access article distributed under the terms and conditions of the Creative Commons Attribution (CC BY) license (<https://creativecommons.org/licenses/by/4.0/>).

1. Introduction

Packaging materials are used to preserve food and minimize food waste throughout the distribution chain [1], with their primary role being barriers against the permeation of small molecules such as oxygen and water, but also grease, germs, and aroma [2]. Petroleum-based polymers are widely used for this purpose owing to their superior combination of permeability, mechanical strength, and low market prices [3,4]. Still, such materials present major sustainability concerns mainly regarding their production routes based on non-renewable raw materials and end of life scenarios. Biobased polymers, such as cellulose-based (e.g., cellophane, cellulose acetate, cellulose ethers), polysaccharides (e.g., starch, chitosan, xylan), and protein-based, have attracted increasing attention as potentially sustainable alternatives. Nevertheless, these materials provide a good barrier against oxygen only below 50% of relative humidity [2,5] and their processing cost remains high. This is the case of microfibrillated cellulose (MFC), which forms a dense network of crystalline nano- and micro-fibrils with intra- and intermolecular hydrogen bonds [6]. MFC films are highly impermeable in the dry state, but the hydrophilic, OH-terminated surface of the fibrils favors the formation of hydrogen bonds with surrounding water molecules. The resulting diffusion of water swells the amorphous regions and increases the interfibril free volume, which in turn increases the permeability of the network and reduces its mechanical stability [7,8]. Etale et al. comprehensively discussed water interactions with cellulose [9].

Several strategies have been developed to improve the barrier and mechanical properties of MFC films at high humidity. These include thermal treatments, a diversity of surface modification approaches such as coating and grafting with polymers, or the addition of high aspect ratio, intrinsically impermeable fillers within the MFC network [10–12]. Magalhaes et al. provided a comprehensive discussion on recent green extraction strategies and chemical surface modification of cellulose derivatives [13]. Saedi et al. conducted a review of physical and chemical surface modifications applied to cellulose, aimed at enhancing the mechanical and barrier properties of cellulose-based composites [14]. Thermal treatments increase the crystallinity and reduce the interfibril distance [15], the water uptake capacity [16], and the oxygen and water vapor permeability [10] in particular at a high relative humidity [11]. Another approach to reduce the sensitivity of the MFC network to moisture is to replace the surface hydroxyls by hydrophobic groups, which has been demonstrated using silylation [17–19], acetylation [20], esterification [21], amidation [22], polymer grafting [23], or using ceric ammonium nitrate for interfacial bonding and encapsulation in a hydrophobic polymer matrix [24]. The addition of impermeable, platelet-type fillers, including hydrophobized graphene oxide [25] and clay [11,26,27], was also shown to efficiently reduce the permeability to gases of cellulose films, typically up to five-fold. Authors claimed that these reductions correlated with an increase in hydrophobicity, which retarded the formation of hydrogen bonds with water molecules and reduced their diffusion rate at the cellulose surface or filler-cellulose interface [10,25]. Researchers have explored other methods to enhance the barrier properties of cellulose-based composites. Nuruddin et al. investigated the potential use of cellulose/polymer coatings for barrier applications [28]. They found that cellulose/PVA films showed exceptional barrier performance, much higher than high-barrier ethylene-vinyl alcohol copolymer films. Additionally, the application of the coating enhanced the oxygen and carbon dioxide barrier performance of PP films. Through the water evaporation-induced dense packing method, Wang et al. produced a high-strength, transparent cellulose film with excellent gas barrier properties [29].

These previous investigations revealed the benefits of specific processes on the diffusion barrier performance of MFC but did not exploit potential synergies between such processes. To this end, the present work explores the role of thermal annealing, the addition of clay, and a fluorine-free hydrophobic silane treatment on the barrier to oxygen and water vapor of MFC films at high relative humidity. Attention is also paid to investigating the impact of these treatments on the microstructure and mechanical properties of the MFC-clay films, and to the interplay between their hydrophobicity and permeability. We demonstrate that the combination of these treatments leads to composite films with superior diffusion barrier performance, in particular at a high relative humidity. The present findings are thus of fundamental value considering the huge effort ongoing worldwide to create bio-based alternatives to conventional oil-based packaging materials, with the main challenge being the need achieve a barrier performance that is comparable to the non-renewable materials [4,30].

2. Materials and Experimental Methods

2.1. Materials and Processes

MFC was supplied in aqueous gel form with a solid content of 10 wt% (Exilva F01-V, Borregaard, Sarpsborg, Norway). The diameter of the MFC fibers was in the range 20 nm–1 μ m (Figure S1 in supplementary information), and their length varied between 5 to 40 μ m [31]. Natural sodium montmorillonite cloisite clay was selected (Cloisite, BYK Additives, Wesel, Germany). The silanes were hexadecyltrimethoxysilane, with C₁₆ alkyl chains (HDTMS, Sigma-Aldrich, Taufkirchen, Germany, 98% purity) and tetraethylorthosilicate (TEOS, Sigma-Aldrich, Germany, 98% purity). Such fluorine-free substances represent a challenge when trying to create superhydrophobic surfaces; however, they come with the benefit of avoiding the potential toxicity related to fluorine. Solvents were ethanol (abcr GmbH, Karlsruhe, Germany) and ammonia hydroxide (Sigma-Aldrich, 99% purity). All products were used as received without further purification.

The MFC suspension was diluted to 0.5 wt% in millipore water and the suspension was homogenized at a speed of 12,000 rpm for 5 min using a high-speed disperser (Ultra-Turrax, IKA, Staufen, Germany). Aqueous clay suspensions (concentration of 0.5 wt%) were prepared using temperature controlled pulsed probe sonication at 30 °C for 5 min with an amplitude 30% and with 5 s on and 5 s off pulses (Branson digital sonifier model 450, Emerson Electric, MO, USA). Specific amounts of MFC and clay to achieve a clay concentration of 10 wt% were mixed under magnetic stirring for 2 h and further homogenized at 12,000 rpm for 10 min. The mixtures were subsequently cast in Teflon petri dishes and left at 30 °C for five days until they formed a film that peeled off from the petri dishes. The samples are denoted in the following as MFC/clay (90/10). The film thickness was measured from cross sectional scanning electron micrographs of films and found to be in the range of 50 to 60 µm. The samples were then annealed in an oven at 150 °C for 3 h, cooled to room temperature, and kept in a desiccator. Some film samples were not subjected to the annealing treatment and were kept as references.

The silylation of the MFC and MFC-clay films was adapted from the one-step sol-gel method described by Medina-Sandoval et al. [17] and Xie et al. [18], who developed superhydrophobic membranes using TEOS to create, in situ, a hierarchical surface roughness and HDTMS as a hydrophobic moiety. In this process a silica sol is formed by hydrolysis of these two silane precursors. A silica gel is subsequently formed from the dehydration and condensation reactions of the hydrolyzed TEOS, which further condenses with the hydrolyzed HDTMS, resulting in hydrophobic alkyl chains attached to the silica gel. In the present work, the MFC and MFC-clay films were immersed in the initial silane solution so that the hydroxyl groups on the cellulose and clay surfaces reacted with the polysiloxane units, leading to the hydrophobization of the films. The hydroxyl groups located at the edges of clays were reported to be the most reactive sites for silane grafting [32,33]. In detail, film samples were soaked for 30 min in a solution prepared by adding TEOS (0.25 g) and HDTMS (0.3 g) into 20 mL of ethanol, followed by dropwise addition of aqueous ammonia (2 mL) under magnetic stirring. The modified films were rinsed with ethanol three times in order to fully remove unreacted moieties and heated to 100 °C for 1 h to promote the condensation of the silanes.

2.2. Characterization Methods

Attenuated total reflectance Fourier transform infrared spectroscopy (ATR-FTIR, Thermo Fisher Scientific Nicolet 6700, Waltham, MA, USA) was used to analyze the surface of the modified films. The spectra were acquired with 32 scans at a resolution of 4 cm⁻¹ in the range 4000–650 cm⁻¹. The surface of the films was investigated by scanning electron microscopy (SEM, ZEISS Gemini SEM 300, Oberkochen, Germany) at an acceleration voltage of 3 kV and a working distance of 5 mm. Prior to SEM analysis, a 10 nm thick layer of gold was sputtered on the film surface to prevent charging effects. The crystal structure of MFC and MFC/clay was investigated by X-ray diffraction (XRD, D8 Discover diffractometer, Bruker AXS, Billerica, MA, USA) with Cu K α radiation (wavelength of 1.542 Å) in reflection mode, and with a step size of 0.02°. Cast films of MFC and MFC/clay and clay in powder form were used. The Origin software was used for data processing, including the subtraction of a blank run from the spectra of the sample, and their normalization with the absolute intensity of the most intense peak. The topography of the films was characterized by atomic force microscopy (AFM, Cypher VRS, Oxford Instrument, Abingdon, UK) in tapping mode with a Si cantilever (AC160TSA). The root mean square roughness (RMS) defined as the RMS average of the height deviations from the mean value was measured on a 2 × 2 µm² area. The water contact angle (WCA) of the films was measured using distilled water and a goniometer (Easy Drop, Krüss, Hamburg, Germany). The goniometer utilizes a backlight and high-resolution camera to capture the image of the sessile drop dispensed by a precision syringe with a volume of 600 µL, from which the WCA is obtained. Dynamic mechanical analysis (DMA, Q800, TA Instruments, New Castle, DE, USA) was performed on the cast films in tensile configuration between 20 °C and 200 °C at a heating

rate of 3 °C min⁻¹, an excitation frequency of 1 Hz, and applied strain of 0.1%. Three samples were tested for each type of film. Tensile testing was performed on rectangular specimens cut from cast films with a 500 N load cell at a nominal speed of 10 mm/min at room temperature (Universal Testing Machine, Schenck Trebel, renewed by Walter&Bai AG, Löhningen, Switzerland). The initial gauge length of the specimens was 25 mm and their width was 10 mm. The oxygen transmission rate (OTR) and water vapor transmission rate (WVTR) of the cast films were measured with a coulometric cell (Systech 8001, Systech Illinois, San Diego, CA, USA) and an electrolytic P₂O₅ cell (Systech 7000, Systech Illinois, California, USA), respectively, using a steel mask with a circular opening of 5 cm². The OTR tests were carried out at 23 °C using pure oxygen and at 50% and 80% relative humidity (RH) and the WVTR tests were carried out at 23 °C and at 50%RH. Two samples were tested for OTR and two different samples were tested for WVTR for each type of films.

3. Results and Discussion

3.1. Structure and Morphology Analysis of MFC-Clay Composite Films

Figure 1a shows the FTIR spectra of reference and heat-treated films. In all cases, the characteristic peaks of cellulose structures are systematically visible (O–H stretching between 3600 and 3300 cm⁻¹, C–H stretching at 2900 cm⁻¹, C–C stretching around 1640 cm⁻¹, CH₂ stretching at 1432 cm⁻¹ and 900 cm⁻¹, C–H bending at 1373 cm⁻¹, asymmetric vibrations of C–O–C and stretching of C–O at 1100, 1053, and 1028 cm⁻¹) [34,35]. The peak intensity at 3325 cm⁻¹ was reduced after heat treatment due to the decrease in the number of free hydroxyl groups, a consequence of the increase of crystalline cellulose [36]. The ratio between the absorbance bands at 3325/1320 cm⁻¹ increased with heat treatment, which has been attributed to increasing intra- and interconnection among the microfibrils via hydrogen bonding [37,38]. A slight shift of the 3325 cm⁻¹ peak to wavenumbers around 3340 cm⁻¹ for the MFC/clay composites was also detected, due to the hydrogen bonding interaction between the OH groups of the clay and MFC [39,40]. Figure 1b shows the spectra of the silylated films. The bands at 2840–2918 cm⁻¹, which correspond to the introduction of alkyl chains, confirmed the successful grafting of HDTMS. The band at 1024 cm⁻¹ corresponds to the asymmetric stretching of the siloxane network on the surface of the modified films, although this peak overlaps with the peak for the MFC C–O bonds. In addition, the band at 791 cm⁻¹ corresponds to Si–O–C stretching from the covalently attached alkyl chains on the surface. This demonstrates that the silylation process of the films surface with HDTMS was achieved [18].

Figure 2 shows the XRD spectra of the clay and the reference and heat-treated films. The silylated films were not investigated as it was shown that this treatment does not change the crystal structure of cellulose in MFC [34]. The clay displays characteristic peaks at 7.5°, 19.6°, 28.6°, and 35.4° corresponding to the (001), (100), (004), and (110) lattice planes of clay, respectively [41,42]. MFC exhibits characteristic peaks around 16° (combined peak) and 22.7°, which correspond to the (1̄10)/(110) and (200) lattice planes, respectively [43], and this structure was not affected by the thermal treatment. For the untreated and annealed MFC/clay films, the (001) peak of clay at 7.5° shifted to a lower angle (6.7°). The interlayer distance, also termed *d*-spacing (*d*₀₀₁), between the clay platelets was calculated using Bragg's equation, and the values are reported in Table 1:

$$n\lambda = 2d_{001}\sin\theta \quad (1)$$

where *n* is the diffraction order, *λ* the wavelength, and *θ* the diffraction angle. The interlayer distance was found to increase in the MFC/clay and heat-treated composites. This was attributed to a partial exfoliation of clay platelets and intercalation of cellulose microfibrils [44]. In addition, the (100) and (004) lateral lattice planes of clay are not visible, which could be due to the fact that the clay platelets are horizontally stacked within the film structure [11].

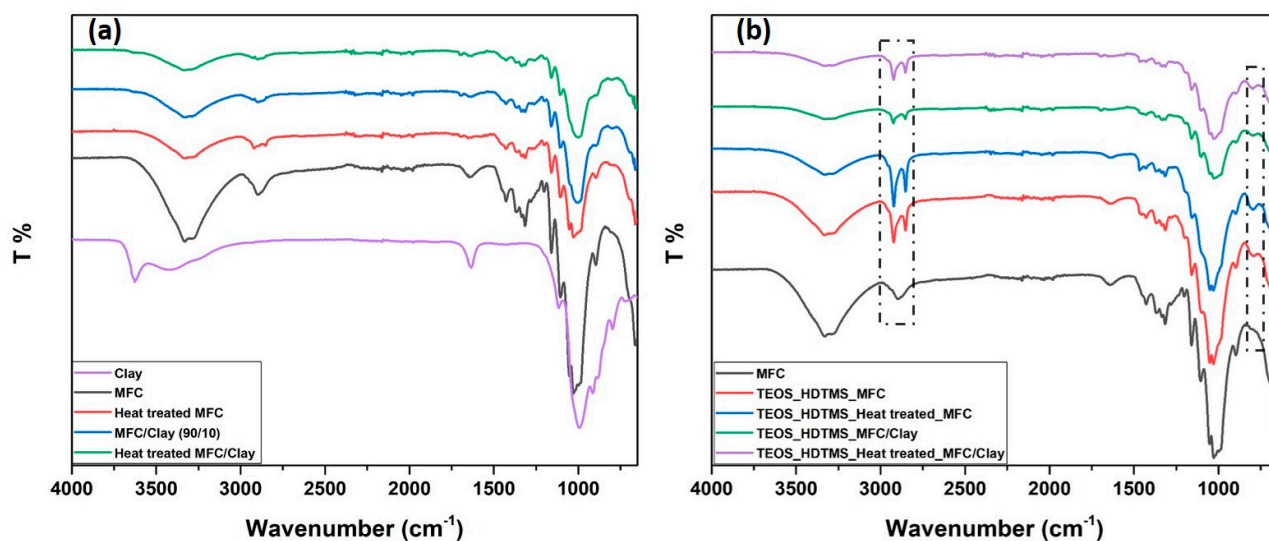


Figure 1. FTIR spectra of clay, MFC, MFC/Clay and heat treated MFC and MFC/Clay films (a) and of TEOS–HDTMS modified MFC, MFC/Clay and heat treated MFC/clay films (b). The presence of alkyl chains ($2840\text{--}2918\text{ cm}^{-1}$) and Si–O–C bonds (791 cm^{-1}) are highlighted in the dashed rectangle areas.

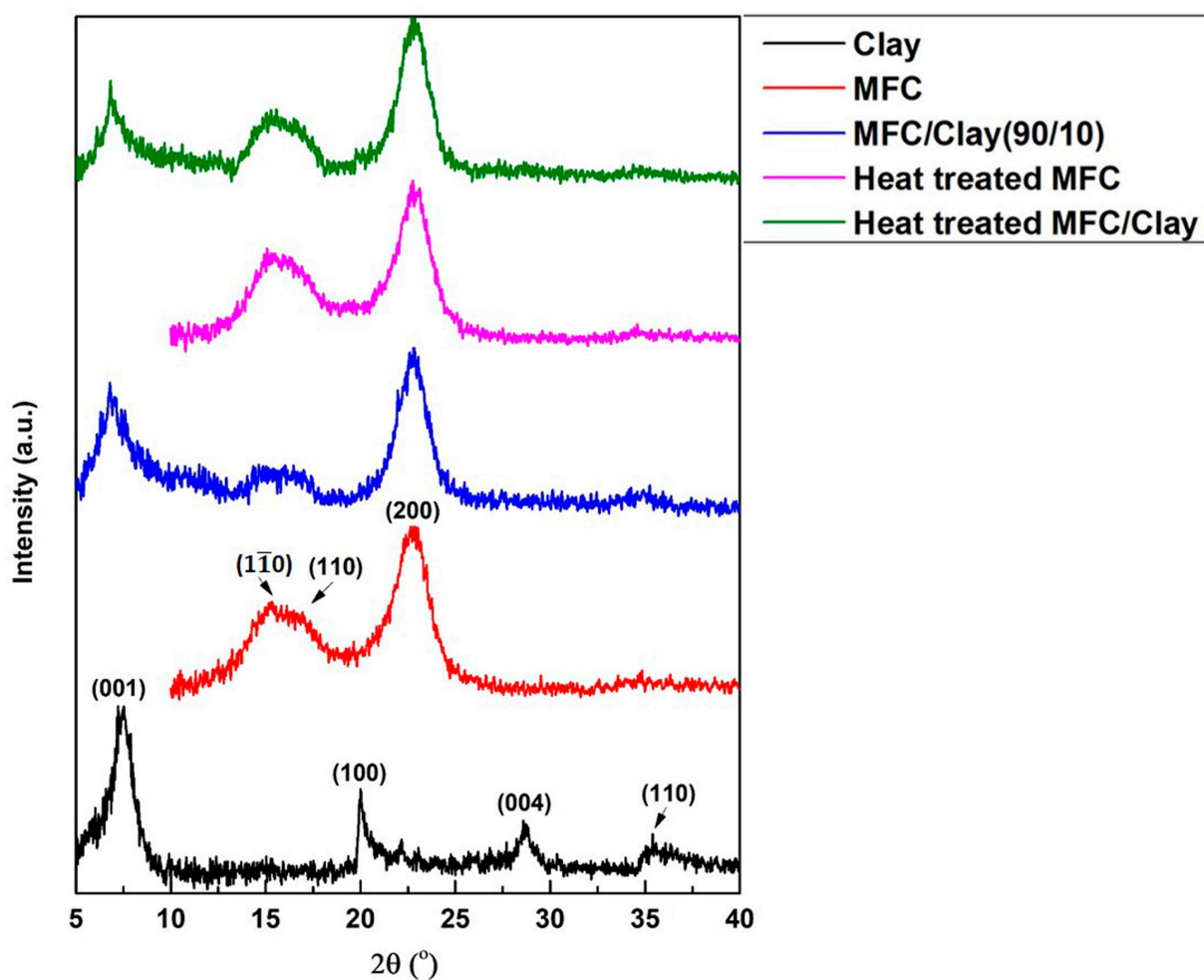


Figure 2. XRD patterns of clay, MFC, MFC/Clay, and heat treated MFC and MFC/Clay films.

Table 1. CI, crystallite size of MFC and d-spacing of clay in MFC-clay films.

Film Material	CI [–]	Crystallite Size <i>D</i> [nm]	d-Spacing <i>d</i> ₀₀₁ [nm]
MFC	0.77	3.83	-
Heat-treated MFC	0.79	3.95	-
Clay	-	-	1.16
MFC/Clay	0.76	3.85	1.32
Heat-treated MFC/Clay	0.78	3.98	1.30

The crystallinity index, CI, of MFC, which provides the relative amount of crystalline material in cellulose, was estimated from the XRD spectra from the widely used empirical method of Segal et al. [45], and the values are reported in Table 1:

$$CI = (I_{22.7} - I_{18})/I_{22.7} \quad (2)$$

where $I_{22.7}$ and I_{18} are the intensities at 2θ of 22.7° and 18° , respectively. The high-intensity peak at 22.7° corresponds to the crystalline fraction. The intensity at the minimum between the (101) and the (002) peaks around 18° was taken as the indicator of amorphous content. The CI of the MFC and MFC/clay films slightly increased after heat treatment, presumably owing to the increase of the cellulose crystallites size. This was checked using the Debye–Scherrer equation [46]:

$$D = K\lambda/\beta\cos\theta \quad (3)$$

where D is the crystallite size, K is the Scherrer constant, and β is the full width of the peak at half maximum intensity (FWHM). As reported in Table 1, the size of the crystallites in the MFC fibers indeed increased upon heat treatment, confirming the co-crystallization mechanism of hornification [10].

Figure 3 shows the electron micrographs of the surface of all investigated films. The reference MFC film (Figure 3a) is characterized by entangled MFC fibers, with no significant morphology changes after heat-treatment (Figure 3b). The clay platelets in the composite film appear to be well-dispersed in the closely packed MFC network (Figure 3c,d). Silica particles are clearly seen on the surface of the silylated films (Figure 3e–g) with a tendency toward aggregation for the heat-treated films (Figure 3f,h).

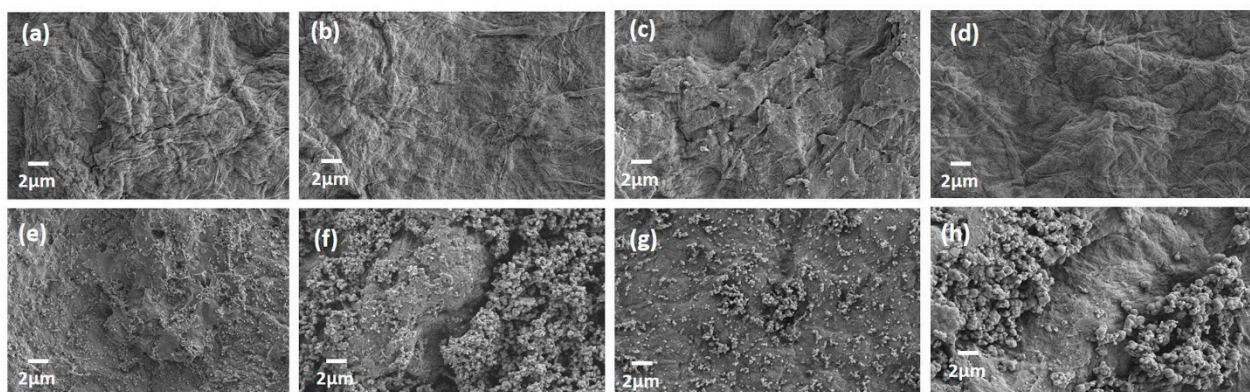


Figure 3. Electron micrographs of MFC (a), heat treated MFC (b), MFC/clay (c), heat treated MFC/clay (d), TEOS-HDTMS modified MFC (e), TEOS-HDTMS modified heat treated MFC (f), TEOS-HDTMS modified MFC/clay (g), and TEOS-HDTMS modified heat treated MFC/clay (h) films.

The AFM topography images are shown in Figure 4 and the values of the measured RMS roughness are reported in Table 2. These images reveal that the surface of the reference MFC film (Figure 4a) is formed by typical random network of nanofibrils while the heat treated MFC film (Figure 4b) shows closely knitted fibrils with increased roughness. The incorporation of clay (Figure 4c) hardly changed the roughness of the film, but again the heat-treated composite films (Figure 4d) were rougher. The roughness largely increased after silylation due to the formation and aggregation of silica particles on the surface of the films (Figure 4e–h).

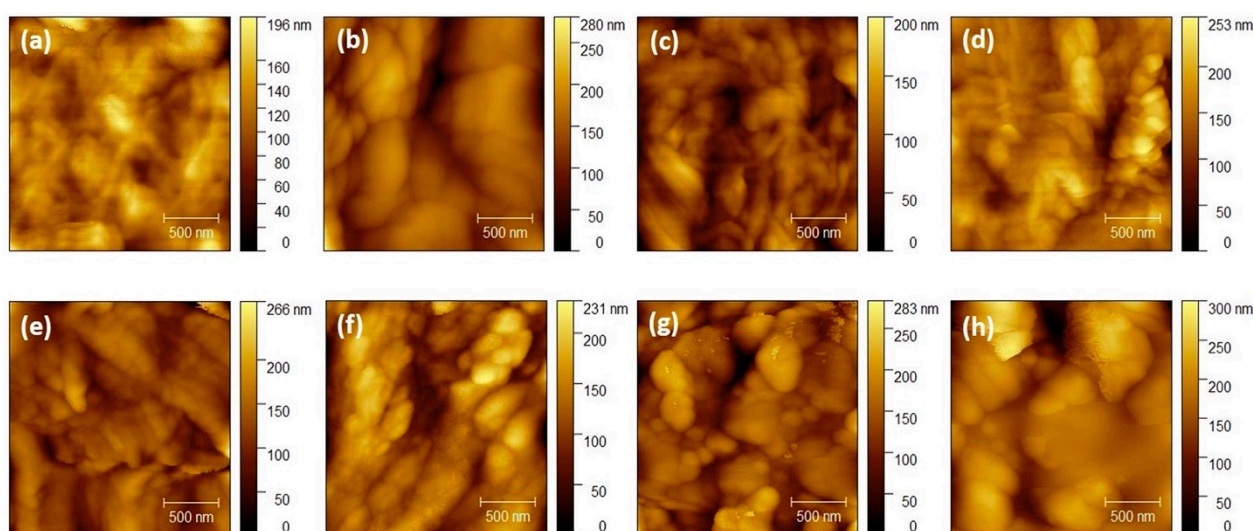


Figure 4. AFM topography images of MFC (a), heat treated MFC (b), MFC/clay (c), heat treated MFC/clay (d), TEOS-HDTMS modified MFC (e), TEOS-HDTMS modified heat treated MFC (f), TEOS-HDTMS modified MFC/clay (g), and TEOS-HDTMS modified heat treated MFC/clay (h) films.

Table 2. RMS roughness and WCA data of MFC and MFC-clay films.

Film Material	RMS Roughness [nm]	WCA [°]
MFC	24.7	39.1 ± 2.5
Heat-treated MFC	35.2	83.5 ± 2.9
MFC/Clay	25.7	50.7 ± 1.4
Heat-treated MFC/Clay	31.1	73.3 ± 2.5
Silylated MFC	25.9	125.1 ± 2.2
Heat treated and silylated MFC	35.4	133 ± 1.3
Silylated MFC/Clay	36.5	138.8 ± 2.3
Heat-treated and silylated MFC/Clay	43.7	146.5 ± 1.0

3.2. Water Contact Angle

Images of water droplets on all investigated films are shown in Figure 5 and corresponding WCA are reported in Table 2. The OH-terminated MFC was hydrophilic with a WCA of 38.5°. After heat treatment, the WCA of the MFC film considerably increased to a value close to the hydrophobic limit of 90°. This was attributed to the increase of the roughness [47,48] and to the decrease in the number of free hydroxyls groups upon heat treatment [16]. The addition of clay also significantly increased the WCA, in this case essentially due to the increase in roughness, and again further heat treatment led to a large WCA increase. The largest increase of WCA was obtained after silylation, up to a value of 146.5° for the heat-treated composite film with non-polar C₁₆ alkyl chains attached over

the surface. This is a remarkable result for a fluorine-free chemistry. This value is close to the superhydrophobic limit of 150° , which indeed required both increased roughness and hydrophobicity of the surface [49].

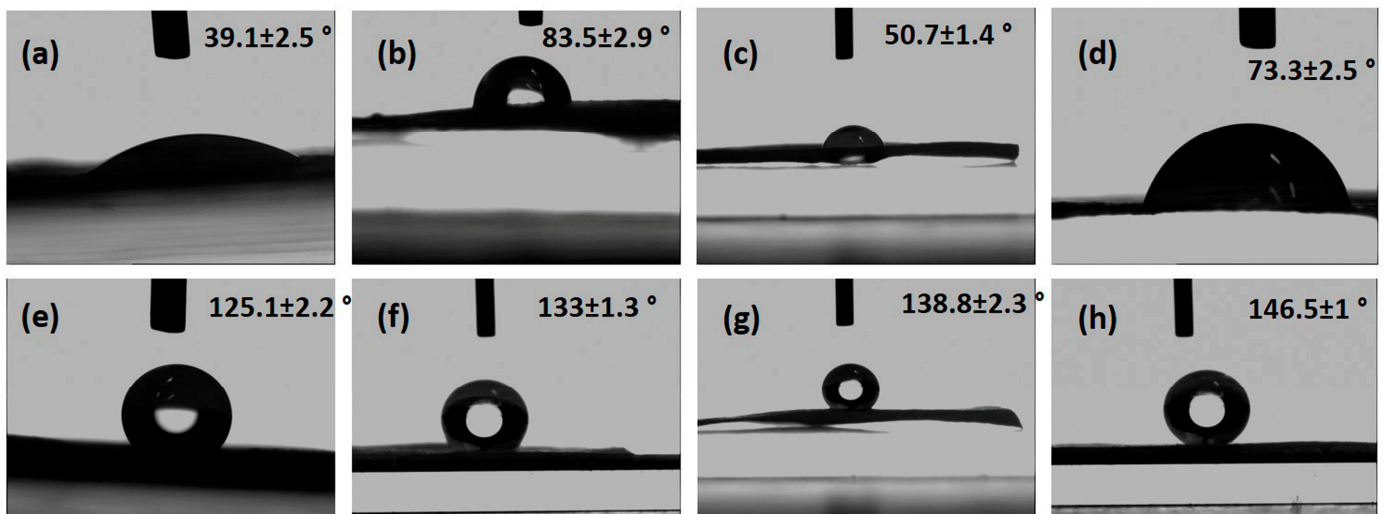


Figure 5. Water droplets and contact angle on MFC (a), heat treated MFC (b), MFC/clay (c), heat treated MFC/clay (d), TEOS-HDTMS modified MFC (e), TEOS-HDTMS modified heat treated MFC (f), TEOS-HDTMS modified MFC/clay (g) and TEOS-HDTMS modified heat treated MFC/clay (h) films.

3.3. Mechanical Analysis

The storage modulus of all films between 20°C and 200°C is shown in Figure 6. The storage modulus of the MFC film was equal to 6.5 GPa at room temperature and gradually decreased to 4.6 GPa at 180°C . These values are lower than what is reported in the literature (8.7 GPa for a clay-MFC film [27]), which may be due to the variation in the MFC fiber size [50,51]. The heat-treated MFC was stiffer, especially at higher temperatures, owing to its improved crystallinity and presumably to the reduction of the inter fibril distance [15]. The modulus of the MFC-clay film was lower at low temperatures (6.2 GPa at 20°C), but the decrease with temperature was less pronounced, with a value of 5.2 GPa at 180°C due to the structural organization and inherent characteristics of clay platelets and mechanically robust cellulose nanofibers. All these effects were rather small, compared with the effect of silylation, leading to a 20% decrease of the modulus for all types of films at low temperature, but an improved stability, especially for the heat-treated film, which modulus was almost constant up to 150°C . Further work is needed to understand such a plasticization effect, which we tentatively attribute to the scission of intermolecular and/or intramolecular hydrogen bonds within the cellulose fibrils upon silylation [52]. This effect was confirmed by the tensile tests shown in Figure S2. These tests also revealed that the high ductility of MFC, with a strain at break around 11%, was reduced with the addition of clay and with the heat treatment, whereas its strength was increased.

3.4. Oxygen and Water Vapor Transmission Rates

Figure 7 shows the OTR of all films at 23°C and at 50%RH and 80%RH, and the WVTR of selected films at 23°C and at 50%RH vs. their WCA values. The OTR of MFC was equal to $1.2\text{ cm}^3/\text{m}^2/\text{day}/\text{bar}$ at 50%RH and increased to $25.3\text{ cm}^3/\text{m}^2/\text{day}/\text{bar}$ at 80%RH. This massive increase results from the disruption and swelling of the H-bonded MFC network by the water molecules as already extensively reported [7,8].

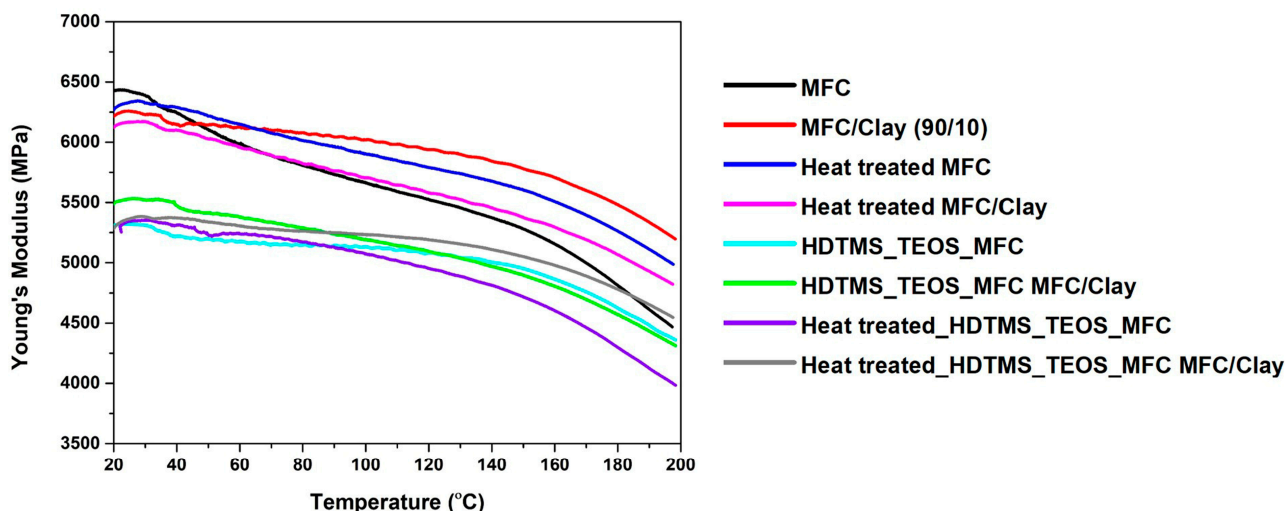


Figure 6. Storage modulus of MFC films, with and without clay, heat treatment and TEOS–HDTMS modification.

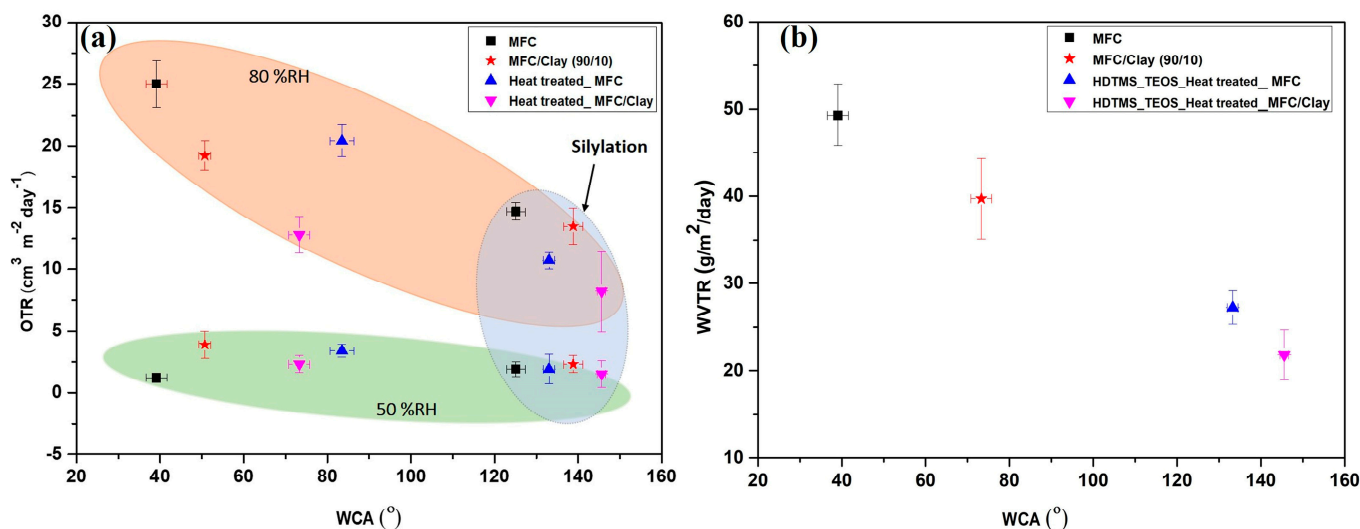


Figure 7. OTR at 23 °C and at 50%RH and 80%RH (a), and WVTR at 23 °C and at 50%RH (b) vs. water contact angle (WCA) of MFC and MFC/Clay films before and after heat treatment and silylation.

The OTR values of all films at 50%RH was in the range of 1.2–3.5 cm³/m²/day/bar irrespective of heat treatment and silylation. Addition of 10 wt% of clay into the MFC led to a 30% reduction of OTR at 80%RH, presumably owing to the creation of a tortuous clay path for oxygen molecules that reduced the permeability beyond a simple linear scaling [11]. The tortuosity is controlled by the orientation and aspect ratio of the individual clay platelets, as defined in the classic Nielsen model for polymer nanocomposites with uniform and impermeable platelets homogeneously dispersed in the matrix [53]:

$$\frac{OTR_{MFC/clay}}{OTR_{MFC}} = \frac{1 - \phi}{1 + \frac{\alpha}{2} \left(S' + \frac{1}{2} \right) \phi} \tag{4}$$

where $OTR_{MFC/clay}$ and OTR_{MFC} are the OTR values of the MFC/clay and MFC films, respectively, ϕ is the volume fraction of clay, α is the aspect ratio, and S' is the orientation factor of the clay platelets. Assuming that the clay platelets are randomly oriented within the MFC network (i.e., $S' = 0$) and that their volume fraction is equal to 5.6% (value calculated from the weight fraction of 10%, assuming a density of clay and MFC equal to

2.8 g/cm³ and 1.5 g/cm³, respectively), one obtains from the OTR values at 80%RH an aspect ratio α equal to 41.8. This value is consistent with a partial exfoliation of the clay particles already detected with the XRD analysis. Indeed, it is much higher than that of the original clay, expected to be close to 1, but much less than that of a fully exfoliated clay with aspect ratio in the range of 100–1000.

Annealing at 150 °C led to a 20% reduction of the OTR of the MFC film at 80%RH to a value of 20.8 cm³/m²/day/bar, and to a 50% reduction to 12.7 cm³/m²/day/bar when it was combined with the addition of clay. The thermal treatment increased the crystallinity and the hydrophobicity of the films due to increased roughness, similarly to previous findings [10]. Silylation further reduced the OTR of the films at 80%RH to a value of 8 cm³/m²/day/bar when combined with clay and annealing, i.e., only five times higher than the OTR at 50%RH, compared with the close to twenty times increase for the pristine MFC. The limited increase of the crystallinity of the cellulose fibrils and the partial exfoliation state of the clay particles had a moderate impact on the barrier improvement, different to the roughening and hydrophobization of the film surface, which played a crucial role in reducing the water adsorption of the films.

Figure 7b shows the correlation between the hydrophobicity of the surface and the WVTR of the film. The WVTR of the pristine MFC film was equal to 49 g/m²/day, which reduced similarly to the OTR with addition of clay, heat treatment, and silylation, to a value of 22 g/m²/day when all these treatments were combined. Kim et al. systematically studied the water adsorption on hydrophilic and hydrophobic surfaces of silicon [54]. They reported that in the case of the hydrophilic, OH-terminated Si surface, water molecules form an ordered network due to strong hydrogen bond interactions with the OH groups. The structure of this H-bonded network gradually changes toward a bulk liquid network as humidity increases. On the contrary, in the case of the H-terminated hydrophobic Si surface, the absence of H-bonds between water molecules and surface leads to physisorbed water molecules H-bonded to each other. In this case the water layer is highly disordered, forming isolated clusters even at high relative humidity. Other investigations show that superhydrophobic surfaces oppose the adsorption of water molecules and thus reduce their diffusion in the bulk [55–57]. Similar phenomena were also observed for droplets of liquid crystalline phase (tactoids). Coalescing tactoids form on hydrophobic surfaces, while hydrophilic surfaces produce base-deposited films of tactoids [58]. The present investigation confirms the favorable influence of hydrophobization on reducing the permeation of water molecules in the MFC network, which also benefits in reducing the permeation of oxygen molecules.

4. Conclusions

Diffusion barrier films based on MFC were developed and the influence of clay particles, thermal annealing, and a fluorine-free silylation on their microstructure, mechanical properties, OTR, and WVTR was systematically investigated. The analysis of the experimental data leads to the following conclusions.

Annealing at 150 °C increased the crystallinity of MFC and decreased the OTR of the MFC films at 80%RH by 20%, from 25.3 to 20.7 cm³/m²/day/bar. It significantly increased the surface roughness and hydrophobicity of the film, with a WCA value of 86.4°. The addition of 10 wt% of clay had no major impact on the crystallinity of MFC and the film surface morphology and properties. However, it led to a 30% decrease of OTR at 80%RH due to a partial exfoliation, and to a 50% decrease when combined with annealing, to a value of 12.7 cm³/m²/day/bar. Silylation did not change the roughness, but considerably increased the surface hydrophobicity of the film with a WCA of 127.5°. The combination of these three treatments further increased the roughness of the film, leading to a WCA of 146.5°, a very high value for a fluorine-free surface that is close to the superhydrophobic threshold. The addition of clay and the thermal treatment did not markedly change the Young's modulus of the MFC film between 20 and 200 °C, and increased the strength at the expense of the ductility. In contrast, silylation led to a 20% decrease of the modulus for all

types of films at low temperature, which remained rather stable up to 150 °C especially for the heat-treated film.

The combination of clay, annealing, and silylation had a limited impact on the OTR of the films at 50%RH, which was in the range 1.2–3.5 cm³/m²/day/bar. However, it considerably reduced the OTR at 80%RH to a value of 8 cm³/m²/day/bar when all treatments were combined. Such a combination also decreased the WVTR of the films at 50%RH, from 49 g/m²/day for MFC to 22 g/m²/day. A correlation was moreover observed between the increase in hydrophobicity of the film surface and the reduction of its OTR and WVTR. This was attributed to the reduced access of water molecules within the MFC network and resulting reduction of the permeation of oxygen molecules.

This research provided insights on specific combinations of processes, which altogether enhanced the barrier properties of MFC-based materials. Results presented in this paper could pave the way to further implementation of biobased and fluorine-free materials towards more sustainable food packaging applications.

Supplementary Materials: The following supporting information can be downloaded at: <https://www.mdpi.com/article/10.3390/surfaces7020019/s1>, Figure S1. AFM image of MFC acquired in tapping mode using a silicon cantilever (AC160TSA) and a Cypher VRS AFM (Oxford Instruments-Asylum Research, USA). Figure S2. Stress-strain curves of MFC films under tensile loading, with and without clay, heat treatment and TEOS-HDTMS modification.

Author Contributions: M.A.P. carried out the experimental investigation and analysis of the data, prepared all figures and wrote parts of the manuscript. Y.L. designed the investigation, analyzed the data and wrote parts of the manuscript. All authors reviewed the manuscript. All authors have read and agreed to the published version of the manuscript.

Funding: The research leading to these results received funding from Société des Produits Nestlé.

Institutional Review Board Statement: Not applicable.

Informed Consent Statement: Not applicable.

Data Availability Statement: The experimental data are available from the corresponding author upon reasonable request.

Acknowledgments: The authors are indebted to the Société des Produits Nestlé for financial support.

Conflicts of Interest: The research leading to these results received funding from the Société des Produits Nestlé.

References

1. Verghese, K.; Lewis, H.; Lockrey, S.; Williams, H. Packaging's Role in Minimizing Food Loss and Waste across the Supply Chain. *Packag. Technol. Sci.* **2015**, *28*, 603–620. [[CrossRef](#)]
2. Helanto, K.E.; Matikainen, L.; Talja, R.; Rojas, O.J. Bio-Based Polymers for Sustainable Packaging and Biobarriers: A Critical Review. *BioResources* **2019**, *14*, 4902–4951. [[CrossRef](#)]
3. Mikkonen, K.S.; Tenkanen, M. Sustainable Food-Packaging Materials Based on Future Biorefinery Products: Xylans and Mannans. *Trends Food Sci. Technol.* **2012**, *28*, 90–102. [[CrossRef](#)]
4. Cazon, P.; Vázquez, M. Bacterial Cellulose as a Biodegradable Food Packaging Material: A Review. *Food Hydrocoll.* **2021**, *113*, 106530. [[CrossRef](#)]
5. Abe, M.M.; Martins, J.R.; Sanvezzo, P.B.; Macedo, J.V.; Branciforti, M.C.; Halley, P.; Botaro, V.R.; Brienza, M. Advantages and Disadvantages of Bioplastics Production from Starch and Lignocellulosic Components. *Polymers* **2021**, *13*, 2484. [[CrossRef](#)] [[PubMed](#)]
6. Lin, N.; Dufresne, A. Nanocellulose in Biomedicine: Current Status and Future Prospect. *Eur. Polym. J.* **2014**, *59*, 302–325. [[CrossRef](#)]
7. Aulin, C.; Gällstedt, M.; Lindström, T. Oxygen and Oil Barrier Properties of Microfibrillated Cellulose Films and Coatings. *Cellulose* **2010**, *17*, 559–574. [[CrossRef](#)]
8. Khazraji, A.C.; Robert, S. Interaction Effects between Cellulose and Water in Nanocrystalline and Amorphous Regions: A Novel Approach Using Molecular Modeling. *J. Nanomater.* **2013**, *2013*, 1–10. [[CrossRef](#)]
9. Etale, A.; Onyianta, A.J.; Turner, S.R.; Eichhorn, S.J. Cellulose: A Review of Water Interactions, Applications in Composites, and Water Treatment. *Chem. Rev.* **2023**, *123*, 2016–2048. [[CrossRef](#)]

10. Sharma, S.; Zhang, X.; Nair, S.S.; Ragauskas, A.; Zhu, J.; Deng, Y. Thermally Enhanced High Performance Cellulose Nano Fibril Barrier Membranes. *RSC Adv.* **2014**, *4*, 45136–45142. [[CrossRef](#)]
11. Bardet, R.; Reverdy, C.; Belgacem, N.; Leirset, I.; Syverud, K.; Bardet, M.; Bras, J. Substitution of Nanoclay in High Gas Barrier Films of Cellulose Nanofibrils with Cellulose Nanocrystals and Thermal Treatment. *Cellulose* **2015**, *22*, 1227–1241. [[CrossRef](#)]
12. Herrera, M.A.; Mathew, A.P.; Oksman, K. Barrier and Mechanical Properties of Plasticized and Cross-Linked Nanocellulose Coatings for Paper Packaging Applications. *Cellulose* **2017**, *24*, 3969–3980. [[CrossRef](#)]
13. Magalhães, S.; Fernandes, C.; Pedrosa, J.F.; Alves, L.; Medronho, B.; Ferreira, P.J.; Rasteiro, M. da G. Eco-Friendly Methods for Extraction and Modification of Cellulose: An Overview. *Polymers* **2023**, *15*, 3138. [[CrossRef](#)] [[PubMed](#)]
14. Saedi, S.; Garcia, C.V.; Kim, J.T.; Shin, G.H. Physical and Chemical Modifications of Cellulose Fibers for Food Packaging Applications. *Cellulose* **2021**, *28*, 8877–8897.
15. Mohan, T.; Spirk, S.; Kargl, R.; Doliška, A.; Vesel, A.; Salzmann, I.; Resel, R.; Ribitsch, V.; Stana-Kleinschek, K. Exploring the Rearrangement of Amorphous Cellulose Model Thin Films upon Heat Treatment. *Soft Matter* **2012**, *8*, 9807–9815. [[CrossRef](#)]
16. Kontturi, K.S.; Kontturi, E.; Laine, J. Specific Water Uptake of Thin Films from Nanofibrillar Cellulose. *J. Mater. Chem. A* **2013**, *1*, 13655–13663. [[CrossRef](#)]
17. Medina-Sandoval, C.F.; Valencia-Dávila, J.A.; Combariza, M.Y.; Blanco-Tirado, C. Separation of Asphaltene-Stabilized Water in Oil Emulsions and Immiscible Oil/Water Mixtures Using a Hydrophobic Cellulosic Membrane. *Fuel* **2018**, *231*, 297–306. [[CrossRef](#)]
18. Xie, A.; Cui, J.; Chen, Y.; Lang, J.; Li, C.; Yan, Y.; Dai, J. One-Step Facile Fabrication of Sustainable Cellulose Membrane with Superhydrophobicity via a Sol-Gel Strategy for Efficient Oil/Water Separation. *Surf. Coatings Technol.* **2019**, *361*, 19–26. [[CrossRef](#)]
19. Guo, N.; Chen, Y.; Rao, Q.; Yin, Y.; Wang, C. Fabrication of Durable Hydrophobic Cellulose Surface from Silane-functionalized Silica Hydrosol via Electrochemically Assisted Deposition. *J. Appl. Polym. Sci.* **2015**, *132*. [[CrossRef](#)]
20. Rodionova, G.; Lenes, M.; Eriksen, Ø.; Gregersen, Ø. Surface Chemical Modification of Microfibrillated Cellulose: Improvement of Barrier Properties for Packaging Applications. *Cellulose* **2011**, *18*, 127–134. [[CrossRef](#)]
21. Wang, Y.; Wang, X.; Xie, Y.; Zhang, K. Functional Nanomaterials through Esterification of Cellulose: A Review of Chemistry and Application. *Cellulose* **2018**, *25*, 3703–3731. [[CrossRef](#)]
22. Gómez, F.N.; Combariza, M.Y.; Blanco-Tirado, C. Facile Cellulose Nanofibrils Amidation Using a ‘One-Pot’ Approach. *Cellulose* **2017**, *24*, 717–730. [[CrossRef](#)]
23. Habibi, Y.; Goffin, A.-L.; Schiltz, N.; Duquesne, E.; Dubois, P.; Dufresne, A. Bionanocomposites Based on Poly (ϵ -Caprolactone)-Grafted Cellulose Nanocrystals by Ring-Opening Polymerization. *J. Mater. Chem.* **2008**, *18*, 5002–5010. [[CrossRef](#)]
24. Galland, S.; Leterrier, Y.; Nardi, T.; Plummer, C.J.G.; Månson, J.A.E.; Berglund, L.A. UV-cured Cellulose Nanofiber Composites with Moisture Durable Oxygen Barrier Properties. *J. Appl. Polym. Sci.* **2014**, *131*, 40604. [[CrossRef](#)]
25. Xu, L.; Teng, J.; Li, L.; Huang, H.-D.; Xu, J.-Z.; Li, Y.; Ren, P.-G.; Zhong, G.-J.; Li, Z.-M. Hydrophobic Graphene Oxide as a Promising Barrier of Water Vapor for Regenerated Cellulose Nanocomposite Films. *ACS Omega* **2019**, *4*, 509–517. [[CrossRef](#)]
26. Singha, S.; Hedenqvist, M.S. A Review on Barrier Properties of Poly (Lactic Acid)/Clay Nanocomposites. *Polymers* **2020**, *12*, 1095. [[CrossRef](#)] [[PubMed](#)]
27. Liu, A.; Walther, A.; Ikkala, O.; Belova, L.; Berglund, L.A. Clay Nanopaper with Tough Cellulose Nanofiber Matrix for Fire Retardancy and Gas Barrier Functions. *Biomacromolecules* **2011**, *12*, 633–641. [[CrossRef](#)] [[PubMed](#)]
28. Nuruddin, M.; Chowdhury, R.A.; Szeto, R.; Howarter, J.A.; Erk, K.A.; Szczepanski, C.R.; Youngblood, J.P. Structure–Property Relationship of Cellulose Nanocrystal–Polyvinyl Alcohol Thin Films for High Barrier Coating Applications. *ACS Appl. Mater. Interfaces* **2021**, *13*, 12472–12482. [[CrossRef](#)] [[PubMed](#)]
29. Wang, Y.; Yuan, L.; Tian, H.; Zhang, L.; Lu, A. Strong, Transparent Cellulose Film as Gas Barrier Constructed via Water Evaporation Induced Dense Packing. *J. Membr. Sci.* **2019**, *585*, 99–108. [[CrossRef](#)]
30. Aulin, C.; Ström, G. Multilayered Alkyd Resin/Nanocellulose Coatings for Use in Renewable Packaging Solutions with a High Level of Moisture Resistance. *Ind. Eng. Chem. Res.* **2013**, *52*, 2582–2589. [[CrossRef](#)]
31. Dalle Vacche, S.; Molina-Gutiérrez, S.; Ladmiral, V.; Caillol, S.; Bongiovanni, R.; Lacroix-Desmazes, P. Photochemical [2+ 2] Cycloaddition of Biobased Latexes for Composites with Microfibrillated Cellulose. *Chem. Eng. Trans.* **2022**, *92*, 277–282.
32. He, H.; Tao, Q.; Zhu, J.; Yuan, P.; Shen, W.; Yang, S. Silylation of Clay Mineral Surfaces. *Appl. Clay Sci.* **2013**, *71*, 15–20. [[CrossRef](#)]
33. Penaloza Jr, D.P. Modified Clay for the Synthesis of Clay-Based Nanocomposites. *Épa. J. Silic. Based Compos. Mater.* **2019**, *71*. [[CrossRef](#)]
34. Poothanari, M.A.; Michaud, V.; Damjanovic, D.; Leterrier, Y. Surface Modified Microfibrillated Cellulose-poly (Vinylidene Fluoride) Composites: B-phase Formation, Viscoelastic and Dielectric Performance. *Polym. Int.* **2021**, *70*, 1316–1328. [[CrossRef](#)]
35. Mohd, N.H.; Ismail, N.F.H.; Zahari, J.I.; Fathilah, W.; Kargazadeh, H.; Ramli, S.; Ahmad, I.; Yarmo, M.A.; Othaman, R. Effect of Aminosilane Modification on Nanocrystalline Cellulose Properties. *J. Nanomater.* **2016**, *2016*, 1–8. [[CrossRef](#)]
36. Korkut, S.; Budakci, M. The Effects of High-Temperature Heat-Treatment on Physical Properties and Surface Roughness of Rowan (*Sorbus Aucuparia* L.) Wood. *Wood Res.* **2010**, *55*, 67–78.
37. Oh, S.Y.; Yoo, D.I.; Shin, Y.; Kim, H.C.; Kim, H.Y.; Chung, Y.S.; Park, W.H.; Youk, J.H. Crystalline Structure Analysis of Cellulose Treated with Sodium Hydroxide and Carbon Dioxide by Means of X-Ray Diffraction and FTIR Spectroscopy. *Carbohydr. Res.* **2005**, *340*, 2376–2391. [[CrossRef](#)] [[PubMed](#)]

38. Abbral, H.; Arikxa, J.; Mahardika, M.; Handayani, D.; Aminah, I.; Sandrawati, N.; Sugiarti, E.; Muslimin, A.N.; Rosanti, S.D. Effect of Heat Treatment on Thermal Resistance, Transparency and Antimicrobial Activity of Sonicated Ginger Cellulose Film. *Carbohydr. Polym.* **2020**, *240*, 116287. [[CrossRef](#)]
39. Jung, B.N.; Jung, H.W.; Kang, D.; Kim, G.H.; Shim, J.K. Synergistic Effect of Cellulose Nanofiber and Nanoclay as Distributed Phase in a Polypropylene Based Nanocomposite System. *Polymers* **2020**, *12*, 2399. [[CrossRef](#)]
40. Li, S.-M.; Jia, N.; Zhu, J.-F.; Ma, M.-G.; Sun, R.-C. Synthesis of Cellulose–Calcium Silicate Nanocomposites in Ethanol/Water Mixed Solvents and Their Characterization. *Carbohydr. Polym.* **2010**, *80*, 270–275. [[CrossRef](#)]
41. Cheng, Y.; Zhang, X.; Xie, W.; Chen, D.; Li, G. The Adsorptive Ability of Ti-Pillared Montmorillonite for Lead (II) Cation. In Proceedings of the 2013 International Conference on Materials for Renewable Energy and Environment, Chengdu, China, 19–21 August 2013; Volume 2, pp. 577–580.
42. Zhirong, L.; Uddin, M.A.; Zhanxue, S. FT-IR and XRD Analysis of Natural Na-Bentonite and Cu (II)-Loaded Na-Bentonite. *Spectrochim. Acta Part A Mol. Biomol. Spectrosc.* **2011**, *79*, 1013–1016. [[CrossRef](#)] [[PubMed](#)]
43. French, A.D. Idealized Powder Diffraction Patterns for Cellulose Polymorphs. *Cellulose* **2014**, *21*, 885–896. [[CrossRef](#)]
44. Wu, C.-N.; Saito, T.; Fujisawa, S.; Fukuzumi, H.; Isogai, A. Ultrastrong and High Gas-Barrier Nanocellulose/Clay-Layered Composites. *Biomacromolecules* **2012**, *13*, 1927–1932. [[CrossRef](#)] [[PubMed](#)]
45. Segal, L.; Creely, J.J.; Martin Jr, A.; Conrad, C. An Empirical Method for Estimating the Degree of Crystallinity of Native Cellulose Using the X-Ray Diffractometer. *Text. Res. J.* **1959**, *29*, 786–794. [[CrossRef](#)]
46. Del Mundo, J.T.; Rongpipi, S.; Yang, H.; Ye, D.; Kiemle, S.N.; Moffitt, S.L.; Troxel, C.L.; Toney, M.F.; Zhu, C.; Kubicki, J.D. Grazing-Incidence Diffraction Reveals Cellulose and Pectin Organization in Hydrated Plant Primary Cell Wall. *Sci. Rep.* **2023**, *13*, 5421. [[CrossRef](#)] [[PubMed](#)]
47. Cassie, A.B.D.; Baxter, S. Wettability of Porous Surfaces. *Trans. Faraday Soc.* **1944**, *40*, 546–551. [[CrossRef](#)]
48. Wenzel, R.N. Resistance of Solid Surfaces to Wetting by Water. *Ind. Eng. Chem.* **1936**, *28*, 988–994. [[CrossRef](#)]
49. Parvate, S.; Dixit, P.; Chattopadhyay, S. Superhydrophobic Surfaces: Insights from Theory and Experiment. *J. Phys. Chem. B* **2020**, *124*, 1323–1360. [[CrossRef](#)] [[PubMed](#)]
50. Gabr, M.H.; Phong, N.T.; Abdelkareem, M.A.; Okubo, K.; Uzawa, K.; Kimpara, I.; Fujii, T. Mechanical, Thermal, and Moisture Absorption Properties of Nano-Clay Reinforced Nano-Cellulose Biocomposites. *Cellulose* **2013**, *20*, 819–826. [[CrossRef](#)]
51. Lu, J.; Wang, T.; Drzal, L.T. Preparation and Properties of Microfibrillated Cellulose Polyvinyl Alcohol Composite Materials. *Compos. Part A Appl. Sci. Manuf.* **2008**, *39*, 738–746. [[CrossRef](#)]
52. Ishimura, D.; Morimoto, Y.; Saito, H. Influences of Chemical Modifications on the Mechanical Strength of Cellulose Beads. *Cellulose* **1998**, *5*, 135–151. [[CrossRef](#)]
53. Choudalakis, G.; Gotsis, A.D. Permeability of Polymer/Clay Nanocomposites: A Review. *Eur. Polym. J.* **2009**, *45*, 967–984. [[CrossRef](#)]
54. Chen, L.; He, X.; Liu, H.; Qian, L.; Kim, S.H. Water Adsorption on Hydrophilic and Hydrophobic Surfaces of Silicon. *J. Phys. Chem. C* **2018**, *122*, 11385–11391. [[CrossRef](#)]
55. Wang, C.; Lai, P.-C.; Syu, S.H.; Leu, J. Effects of CF₄ Plasma Treatment on the Moisture Uptake, Diffusion, and WVTR of Poly (Ethylene Terephthalate) Flexible Films. *Surf. Coat. Technol.* **2011**, *206*, 318–324. [[CrossRef](#)]
56. Zhou, S.-Y.; Yang, B.; Li, Y.; Gao, X.-R.; Ji, X.; Zhong, G.-J.; Li, Z.-M. Realization of Ultra-High Barrier to Water Vapor by 3D-Interconnection of Super-Hydrophobic Graphene Layers in Poly(lactide) Films. *J. Mater. Chem. A* **2017**, *5*, 14377–14386. [[CrossRef](#)]
57. Jiang, X.; Li, Q.; Li, X.; Meng, Y.; Ling, Z.; Ji, Z.; Chen, F. Preparation and Characterization of Degradable Cellulose–Based Paper with Superhydrophobic, Antibacterial, and Barrier Properties for Food Packaging. *Int. J. Mol. Sci.* **2022**, *23*, 11158. [[CrossRef](#)]
58. O’Keeffe, O.; Wang, P.-X.; Hamad, W.Y.; MacLachlan, M.J. Boundary Geometry Effects on the Coalescence of Liquid Crystalline Tactoids and Formation of Topological Defects. *J. Phys. Chem. Lett.* **2019**, *10*, 278–282. [[CrossRef](#)]

Disclaimer/Publisher’s Note: The statements, opinions and data contained in all publications are solely those of the individual author(s) and contributor(s) and not of MDPI and/or the editor(s). MDPI and/or the editor(s) disclaim responsibility for any injury to people or property resulting from any ideas, methods, instructions or products referred to in the content.